Available online at www.sciencedirect.com
ScienceDirect
Journal of Power Sources 164 (2007) 829–838
JOURNAL OF POWER SOURCES
www.elsevier.com/locate/jpowsour

Synthesis and characterization of electrochemically active graphite–silicon–tin composite anodes for Li-ion applications

Nicolaus L. Rock [a], Prashant N. Kumta [a,b,*]

[a] *Department of Materials Science and Engineering, Carnegie Mellon University, Pittsburgh, PA 15213, USA*
[b] *Department of Biomedical Engineering, Carnegie Mellon University, Pittsburgh, PA 15213, USA*

Received 3 October 2006; received in revised form 24 October 2006; accepted 25 October 2006
Available online 13 December 2006

Abstract

Electrochemically active $Si_{0.66}Sn_{0.34}$ (SiSn) composite alloys dispersed in a carbon (graphite) matrix were synthesized using both wet and dry high-energy mechanical milling (HEMM). The resultant composites are comprised of amorphous carbon (in the case of dry HEMM) or crystalline carbon (in the case of wet HEMM), and crystalline silicon and tin (for both cases) as verified by X-ray diffraction (XRD). The XRD results also indicate the presence of iron–tin intermetallic ($FeSn_2$) arising as a contaminant during dry HEMM. The composite composition of 85C–15[$Si_{0.66}Sn_{0.34}$] (mol%) resulted in reversible discharge capacities as high as 800 mAh g^{-1} with a reasonable capacity retention (1.36% loss/cycle). Scanning electron microscopy (SEM) and Fourier transform infrared spectroscopy (FTIR) analyses were further conducted to examine the surface of the electrode and to determine the presence/absence of organic species resulting from reactions between the electrode, lithium ions and electrolyte, respectively.

Keywords: High-energy mechanical milling; C–SiSn composite; Anode; Li-ion battery

1. Introduction

Since Sony commercialized the first rechargeable lithium-ion (Li-ion) battery in 1991 [1], it has emerged as the most promising energy system for fulfilling the diverse needs of device manufacturers. Although Li-ion batteries are at the forefront of battery technology, there is an ever-growing need to improve the energy density. A number of cathode and anode systems have also been studied and more recently, alternative anode materials have become a major focus. Carbon has been the standard anode material to date, exhibiting a reversible capacity of 372 mAh g^{-1} [2]. This relatively low capacity illustrates the need to identify improved anode systems to meet the challenging energy storage demands of emerging and existing technologies. Much work has been directed towards developing alternative anodes, specifically focused on Si and Sn systems, since they possess large theoretical capacities of 4197 and 994 mAh g^{-1}, respectively [3]. However, the main problem with these metals is upon alloying with lithium, they undergo major changes in structure and volume. This results in a brittle alloy which experiences a significant volume change (300–600%) between the unalloyed and alloyed states [4]. As a consequence, mechanical stresses build up resulting in cracking and crumbling of the electrode and loss of inter-particle electronic contact. This leads to capacity loss with cycling resulting in rapid failure of cells [4–11]. One solution to this problem that was actively pursued is the generation of active–inactive nanocomposites containing the electrochemically active phase embedded in an electrochemically inactive phase [12].

Disordered carbon generated by pyrolysis of polymers was thus used to produce nanodispersed silicon in a carbon matrix yielding reversible specific capacities up to 600 mAh g^{-1} [13–15]. Similar research by Kim et al. on tin particles dispersed within an amorphous carbon matrix has yielded reversible capacities as high as 500 mAh g^{-1} [16]. Kim et al. have also demonstrated that amorphous silicon can be contained within nanocrystalline matrices of TiN, TiB_2 and SiC to successfully generate stable reversible capacities up to 400 mAh g^{-1} [17,18]. Additionally, there has been some success reported

* Corresponding author at: Department of Materials Science and Engineering, Carnegie Mellon University, Pittsburgh, PA 15213, USA. Tel.: +1 412 268 8739.
E-mail address: kumta@cmu.edu (P.N. Kumta).

0378-7753/$ – see front matter © 2006 Published by Elsevier B.V.
doi:10.1016/j.jpowsour.2006.10.068

on Si dispersed in C including carbon nanotubes (CNT) [14,15,19–35].

The concept of generating active phases in an inactive spectator phase led to the development of unique composites [12,19,27–43]. However, the systems are affected by either large irreversible losses or inferior gravimetric capacities and subsequent capacity fade [12,19,32–43]. Thus, there is a critical need to identify new materials and approaches to capitalize on the large theoretical capacity of Sn and Si. The generation of a nanocomposite containing Si and Sn dispersed in a relatively inactive matrix such as C is potentially worth exploring due to the following advantages. First, the high theoretical capacities of both Si and Sn can be combined in this composite structure thus allowing the potential of generating higher capacity than C and Sn/C composites. Second, as Si and Sn are immiscible and Sn is significantly more ductile than Si, the introduction of Sn has the ability to coat the Si particles and reduce the interaction of Si with C (graphite). Since Sn does not react with C (graphite), it can reduce SiC formation as it will act as a diffusion barrier that would prevent the reaction between Si and C. Third, the soft ductile nature of graphite may act as an excellent binding agent for this composite, while also enduring the extreme strains that result from the large volume changes due to the expansion of Si and Sn upon insertion and de-insertion of lithium.

For this study, therefore, composite systems containing silicon–tin ($Si_{0.66}Sn_{0.34}$) in percentage ratios ranging from 10 to 25% (mol%) with the balance of graphite have been studied. The ratio of $Si_{0.66}Sn_{0.34}$ was chosen based upon the work conducted previously by Beaulieu et al. [44], which focused on sputter deposition, and shows that this ratio of silicon to tin is quite promising. The composites in the present study were generated using a SPEX 8000 shaker mill, wherein the active elements of Si and Sn are homogeneously distributed within the graphite matrix. The present manuscript describes the results of these studies.

2. Experimental details

2.1. Materials synthesis

There were two types of HEMM used for the present study, dry and wet HEMM. Dry milling is the milling/mixing of dry precursors with milling media inside the vial. Wet milling is similar, the only difference being that a solvent is used along with the milling media and the dry precursors. All powders were handled inside an ultra-high-purity (UHP) argon filled glove box (VAC atmosphere, Hawthorne, CA, O_2 and moisture content < 10 ppm). The powders [Si (Alfa Aesar, 99.5%, 325 mesh), Sn (Alfa Aesar, 99.8%, 325 mesh), synthetic graphite (Aldrich, 99.9%, 1–2 μm)] were weighed using a Mettler-Toledo balance (±1 mg) and placed into an air tight round-ended hardened steel vial (SPEX CertiPrep model 8009) with eight steel balls (1/4 in. diameter) inside the glove box. The amount of sample used in each experiment was ∼2 g. The mass of the milling media was slightly more than 16 g, giving an approximate ball to charge ratio of 8:1. For wet HEMM only the materials used to create the electrode slurry namely, polyvinylidene fluoride (PVDF), *N*-methylpyrrolidinone (NMP) and Super P carbon black (Erachem, Europe; surface area ∼ 62 $m^2\,g^{-1}$) were added in with the rest of the powders. In both wet and dry HEMM, the active material was mixed with carbon black and PVDF in the ratio of 10.25:1.25:1 by weight (see Tables 1 and 2 for a list of the synthesized compositions). The milling media and sample were covered with ∼3 mL of solvent so that the level was just high enough to cover the powders. The vial was closed and then taken from the glove box and placed into a SPEX CertiPrep 8000M mixer/mill (frequency = 20 Hz) and milled for 5 or 10 h (both wet and dry HEMM). This was done at intervals of 2 h with a 30 min rest in between each cycle. For wet HEMM only, the vial was opened two to three times during the milling process to ensure that adequate solvent was present to cover the powder samples for the completion of the wet milling process. Once the

Table 1
Comparison of electrochemical performances of C–Si–Sn composite materials

Sample	First cycle insertion capacity (mAh g^{-1})	First cycle de-insertion capacity (mAh g^{-1})	Irreversible loss (%)	Loss per cycle (%)	End capacity (30 cycles) (mAh g^{-1})
75-D-10	1452	849	∼41.5	∼2.94	∼100
80-W-10-N	1082	560	∼48.2	∼0.96	∼400
85-W-10-N	1693	704	∼58.4	∼1.12	∼470
90-D-10	818	441	∼46.0	∼0.60	∼370

D: dry; W: wet; N: NMP.

Table 2
Comparison of electrochemical performances of the 85C–15[$Si_{0.66}Sn_{0.34}$] (mol %) composition at varying milling times, conditions and solvents

Sample	First cycle insertion capacity (mAh g^{-1})	First cycle de-insertion capacity (mAh g^{-1})	Irreversible loss (%)	Loss per cycle (%)	End capacity (30 cycles) (mAh g^{-1})
85-D-10	516	314	∼39.2	∼0.55	∼260
85-W-10-T	1518	616	∼59.4	∼1.25	∼385
85-W-5-T	1600	792	∼50.5	∼1.36	∼470
85-W-10-N	1693	704	∼58.4	∼1.12	∼470

D: dry; W: wet; N: NMP; T: toluene.

milling process was complete, the sample was collected from the vial in air. The various sample compositions, milling times and conditions, are designated as XX-Y-ZZ-A, where 'X' represents the sample composition, 'Y' the type of milling, 'Z' the milling time in hours and 'A' is the solvent that was used during the milling process. For example, 85-W-10-T would translate to 85C–15[$Si_{0.66}Sn_{0.34}$], wet HEMM for 10 h in toluene. 'W' and 'D' are used to indicate wet and dry HEMM, respectively, and 'N' and 'T' are used to indicate NMP and toluene, respectively.

2.1.1. Battery slurry casting and drying

In order to evaluate the electrochemical characteristics, electrodes were fabricated by mixing 82 wt.% of the active powder obtained by dry HEMM of ~325 mesh and 10 wt.% Super P carbon black. A solution containing 8 wt.% polyvinylidene fluoride in *N*-methylpyrrolidinone was added to the mixture containing the powder obtained by dry HEMM. For wet HEMM the active powder, Super P, PVDF and NMP are all present (in the same ratios used to prepare the electrodes) within the milling vial and the action of HEMM provides more than adequate mixing to form a castable slurry. In both cases, the electrode is made by roll casting the resulting slurry produced from the mixing of these materials using a magnetic stir bar or from the milling process, mentioned above. This well-mixed slurry is cast onto a copper foil (INSULECTRO, electro-deposited, thickness: 175 μm) using a roller, to form a thin, even coating. The electrode is then allowed to dry in air for a minimum of 6 h. This dried product is then punched into a 1 cm^2 disk (to be used as electrodes), and then vacuum dried at 100 °C for a minimum of 12 h to remove any remaining moisture. After completely drying, the electrodes are moved into an argon filled glove box (VAC atmosphere, Hawthorne, CA, O_2 and moisture content < 10 ppm) for assembling the test cells.

2.2. Materials characterization

2.2.1. X-ray diffraction (XRD) of the as milled powder samples

X-ray scans were performed on the composite materials. The phases present in the milled samples were analyzed by X-ray diffraction incorporating a state-of-the-art detector (Philips PW3040PRO, θ/θ powder diffractometer with X'celerator detector and Cu Kα radiation source, λ = 0.15406 nm). The milled powder samples were loaded into a top-loaded sample holder made from aluminum with a glass slide affixed to the bottom. Once enough powder was placed into the holder, the powder was leveled off using a glass slide and a scan was taken. Typical scans were recorded in the range $2\theta = 10–90°$. The scan time was 60 min with a step size of 0.008, time per step of 46.99 s and a scan speed of 0.023° s^{-1}.

2.2.2. Fourier transform infrared spectroscopy (FTIR)

FTIR was performed on the samples cycled for 1, 5 and 25 cycles, that had been washed with dimethyl carbonate (DMC) inside the UHP-Ar glove box for 24 h to remove the presence of any remaining lithium containing electrolyte in the electrodes. They were then dried in a vacuum oven at 90 °C for 24 h to remove any excess solvent. The samples were mixed with KBr in a ratio of 1:100, respectively. A pellet was prepared by pressing the dried, milled sample to 3000 psi for 2 min using a Carver 10 ton hand operated press. A Mattson Galaxy Series FTIR 5000 in transmission mode was used to collect the spectra in the scan range of 400–4000 cm^{-1}.

2.2.3. Scanning electron microscopy (SEM)

The cycled samples were first washed with DMC for 24 h inside the UHP-Ar glove box to remove the presence of any remaining lithium containing electrolyte (conducted inside the UHP-Ar glove box). They were then dried in a vacuum oven at 90 °C for 24 h to remove any excess solvent. To investigate the microstructure of the as prepared composites as well as the electrochemically cycled sample, scanning electron microscopy analysis was conducted. A Philips XL30 scanning electron microscope operating at 20 kV was employed for the SEM analysis.

2.2.4. Electrochemical characterization

A "hockey-puck" cell was used for the characterization of the electrochemical properties as reported in the literature [45]. The hockey-puck cell is a three-electrode cell that includes a ring shaped lithium reference electrode. It is important to note that this setup is a "half-cell" setup and the lithium foil counter electrode is the true anode. The reference electrode is placed nearby the edge of the cathode (Si–Sn–C sample) in order to measure the exact voltage of the electrode while a glass fiber separator (Whatman GF/D) is located between the cathode and anode. A liquid electrolyte consisting of 1 M $LiPF_6$ in ethylene carbonate/dimethyl carbonate (EC/DMC) with a molar ratio of EC:DMC = 2:1 is used for the test. All hockey-puck batteries were cycled under constant current charge/discharge conditions using a galvanostat (BT-2000, Arbin Instruments, Texas). Tests were conducted employing constant current densities of 250 μA cm^{-2}. All of the batteries tested in this study were cycled in the voltage range 0.02–1.2 V with a 60 s rest period between each charge/discharge half cycle.

3. Results and discussion

3.1. X-ray characterization

3.1.1. Dry HEMM

Fig. 1 shows the X-ray plot of all four compositions. Amorphization of graphite was a significant occurrence in those samples dry milled for extended periods of time. This is evident due to the lack of a graphite peak seen in both the dry milled 75-D-10 and 90-D-10 scans (Fig. 1). $FeSn_2$ peaks are present in these two composites as a result of contamination arising from the stainless steel vial and subsequent alloying between the Sn and Fe particles present, facilitated by the high impact energy during the dry HEMM process. However, the Sn present in $FeSn_2$ is known to be active, thus Sn is not lost as a result of forming this alloy [12].

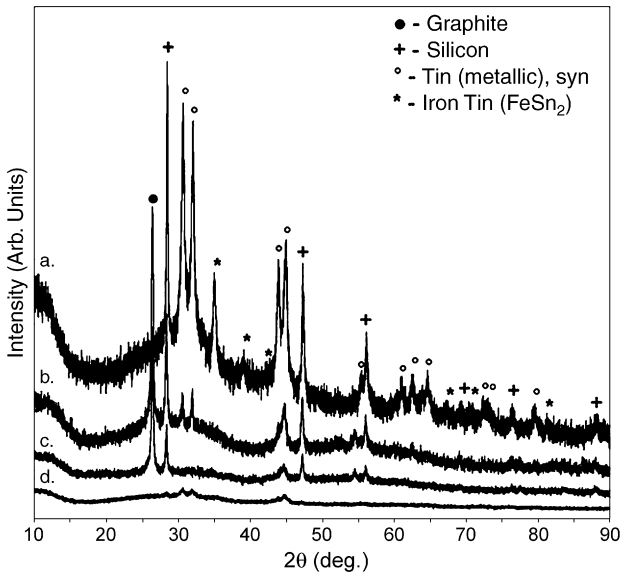

Fig. 1. XRD patterns of C–Si–Sn composites: (a) 75-D-10, (b) 80-W-10-N, (c) 85-W-10-N and (d) 90-D-10.

3.1.2. Wet HEMM

In the 80-W-10-N and 85-W-10-N samples well-defined crystalline graphite peaks can be seen at $2\theta = 26.5^\circ$ and 54.5°, indicating that for these two wet milled samples, amorphization of graphite was not a significant occurrence. There are no crystalline tin oxide (SnO) peaks present in any of the scans; however, the possibility of presence of amorphous SnO in both the 80-W-10-N and 85-W-10-N samples cannot be discounted, as will be described below. In all of the scans collected on wet milled samples there is some amorphization of the graphite as well as Sn and Si which is indicated by the broadening of the characteristic peaks for each element.

The above two compositions were wet milled in NMP which contains a double-bonded oxygen within its structure (C_5H_9NO). It is therefore possible that SnO is formed due to the interaction of NMP with Sn due to cleavage of the doubly bonded oxygen in NMP. Although XRD did not show the presence of any crystalline SnO, FTIR analysis conducted, the results of which are discussed later, could also indicate the presence of any amorphous SnO phases present in the system. Due to the high impact energies that arise during HEMM, it is possible that the oxygen bonded to NMP reacts with the Sn particles. Since the oxygen is doubly bonded and the amount of Sn is very small, the extent of reaction between the two will most likely be limited.

It is also important to note that there is no formation of any crystalline silicon carbide (SiC) in any of the wet or dry milled composites. Due to the high energy involved in HEMM, formation of crystalline SiC is quite possible [46,47]. However, formation of amorphous SiC (a-SiC) is unlikely, as the high impact energy of HEMM will most likely help to form crystalline SiC by diffusion induced reaction of Si and C particles similar to published reports [48]. SiC is also a very hard material and the milling energy using steel balls as the milling media is unlikely to cause any amorphization. Reports of work performed on the Si–SiC and Si–C system by Kim et al. reinforces this claim [46,47]. Kim et al. also showed the formation of crystalline SiC when Si and C were dry milled, but in the experiments performed here, crystalline SiC does not form [46]. This may be attributed to the wet milling process as well as the presence of Sn. Wet milling can drastically reduce the energy available for SiC formation and the presence of Sn in the milling vial could act as a diffusion barrier between Si and graphite since Sn is immiscible in Si.

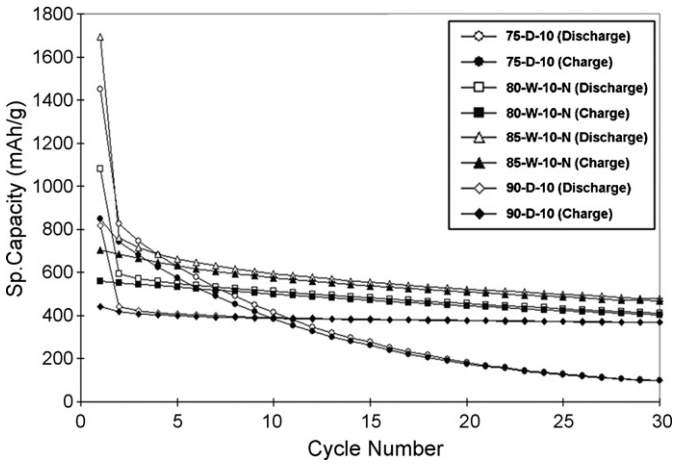

Fig. 2. Specific capacity vs. cycle numbers of C–Si–Sn composite materials cycled at a rate of 250 μA cm^{-2}.

3.2. Electrochemical characterization

Each material was electrochemically tested for 30 cycles. All the samples were cycled at a rate of 250 μA cm^{-2}. Fig. 2 compares the cycling data for all four composites tested. Table 1 summarizes the results of their electrochemical performance. The composition, 85-W-10-N that was obtained by wet milling yields the best overall performance as it exhibits a moderately low loss per cycle of ∼1.12 with a capacity of ∼470 mAh g^{-1} after 30 cycles. In examination of the differential capacity plots of this composite (Figs. 3 and 4), one can see that there are peaks corresponding to the reaction of Li-ions with Si at ∼0.45, 0.3,

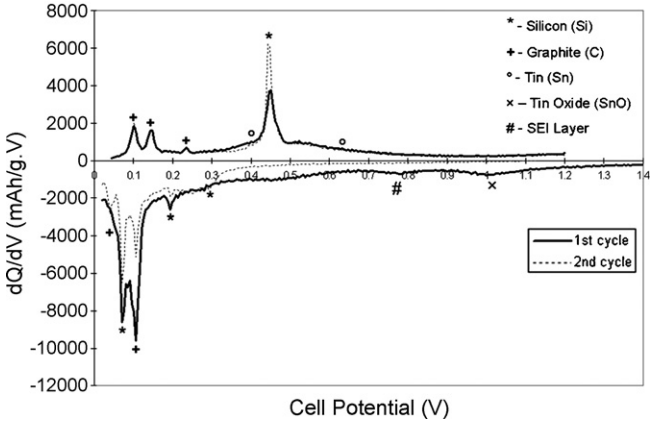

Fig. 3. Differential capacity vs. cell potential curves of 85-W-10-N after first and second cycles.

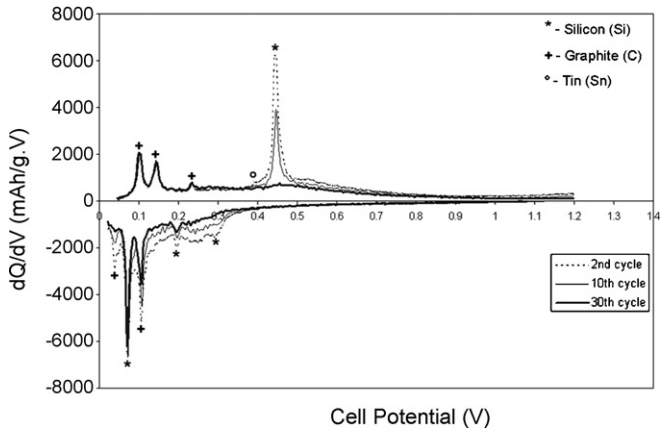

Fig. 4. Differential capacity vs. cell potential curves of 85-W-10-N after 2nd, 10th and 30th cycles.

0.2 and 0.08 V [46]. There are also peaks present for graphite at ∼0.22, 0.15, 0.10 and 0.07 V [49]. The broad peak that is present between 1.0 and 1.4 V (Fig. 3) is indicative of reduction of amorphous SnO by Li suggesting the presence of SnO [50]. The peaks for alloying of Li with crystalline Sn, 0.66, 0.53, 0.49, 0.42 and 0.38 V [49] appear faintly in the $dQ\,dV^{-1}$ plot, being barely noticeable near 0.38 and 0.66 V. This may be due to the fact that there is very little Sn in both compositions and thus the reaction of Li-ions with Sn is limited as compared to the reactions of Li-ions with Si and graphite. The formation of an SEI layer is seen by the presence of a small but broad peak between 0.76 and 0.86 V in Fig. 3 [49]. The presence of the SEI layer is also evident in the suppression of the first cycle lithium intercalation below the *x*-axis in these plots, which can extend beyond the potential of the broad peak seen in the $dQ\,dV^{-1}$ plots [49]. The theoretical specific capacity of 85-W-10-N has been calculated as 1128 mAh g^{-1}. This composite exhibits a first cycle capacity insertion above theoretical which can be attributed to the formation of the SEI which will be explained below.

In all of these materials there is a significant amount of irreversible loss. This is easily seen by the large difference in specific capacity in the 1st cycles of each composite, illustrated in Fig. 2. This loss can also be seen by the difference between the first cycle and subsequent cycles in the $dQ\,dV^{-1}$ plots given for 85-W-10-N (Figs. 3 and 4). This irreversible loss is based upon the difference between the amount of Li that is inserted into the anode upon intercalation into carbon and alloy formation with $Si_{0.66}Sn_{0.34}$ and how much is extracted again upon removal of lithium. The cause for this irreversible consumption of lithium can result from the reaction with the electrolyte causing decomposition and irreversible charge, reduction of impurities in the battery, including H_2O and O_2, reduction of "surface complexes" such as "surface oxides", and lithium incorporation into the carbon matrix by irreversible reduction of "internal surface groups" at prismatic surfaces of domain boundaries in polycrystalline carbons such as graphites [51].

3.3. FTIR analysis

As mentioned above there exists a film that covers the anode called the solid electrolyte interphase (SEI) layer. This layer may be comprised of many different phases depending upon the species involved in electrochemical cycling. It is known that a liquid electrolyte consisting of 1 M $LiPF_6$ in ethylene carbonate/dimethyl carbonate when used opposite a graphite anode, the SEI layer is mainly comprised of LiF, Li_2CO_3 and some Li_2O [49]. In the current study, graphite is used along with the same type of electrolyte. Comparison of the results obtained in this work with published reports on similar systems [52–54], combined with the data obtained using FTIR to study the 85-W-10-N composite material (Fig. 5), it can be seen that alkyl lithium carbonates, ($ROCO_2Li$), lithium carbonate (Li_2CO_3), ethylene

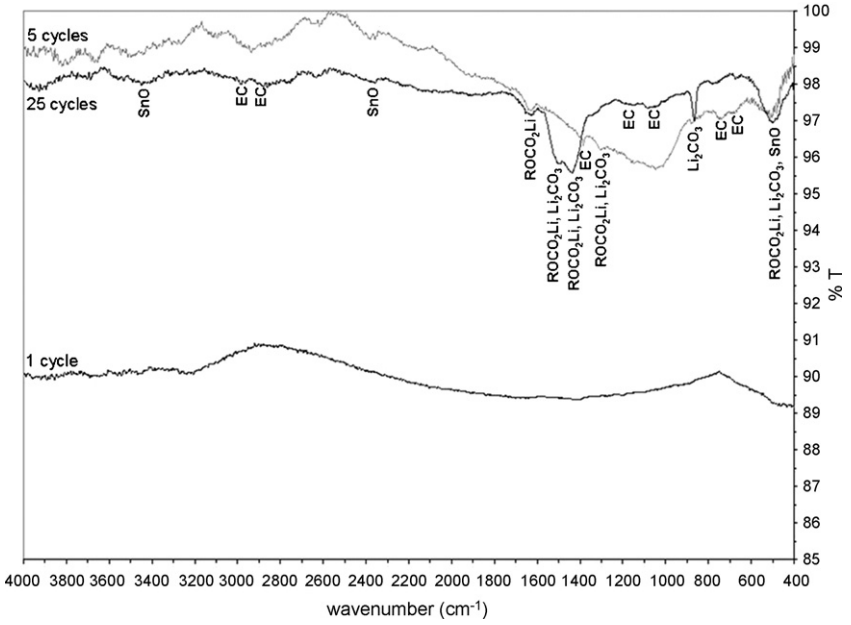

Fig. 5. FTIR transmission mode plots of 85-W-10-N after 1st, 5th and 25th cycles.

carbonate (EC), and tin oxide (SnO) were found to be present in the electrode cycled for 25 cycles. EC will tend to react with lithium ions to form $ROCO_2Li$ which are attached to the graphite surface planes. These will then react with trace H_2O adsorbed on the surface of the electrode to form Li_2CO_3. Though not seen here, Li_2O can also form as a result of the interaction of LiOH with H_2O or reaction of Li-ions with O_2 adsorbed on the surface of the anode or the electrolyte.

All of these materials, while being good Li-ion conductors, trap lithium permanently, which then contributes to the irreversible loss seen in the materials presented here as well as in the reports of the work reported in the literature [51]. The fact that the SEI layer is comprised of lithium containing species also accounts for the occurrence of greater than theoretical first cycle insertion capacities since theoretical capacities are based upon the active material that can undergo lithiation. Since there is reaction of Li-ions within the SEI layer as well, this creates the additional specific capacity above the theoretically calculated value. The reason for the delayed appearance of these peaks may be due to the thickening of the SEI layer with each cycle, thus allowing for the presence of a greater concentration of these species and subsequently greater visible peak intensity.

As stated previously, tin oxide materials have been used as anodes for Li-ion secondary batteries [55]. It is interesting to note here that one of the reactions that occurs during the discharge cycle when Li-ions are being inserted into the structure results in the formation of Li_2O, indicating reduction of the oxide by the lithium ions [50].

$$SnO + 2Li^+ + 2e^- \rightarrow Sn + Li_2O$$

Based upon this reaction and the fact that amorphous SnO exists in both the 85-W-10-N (see Fig. 5) and 80-W-10-N composites, it can be inferred that SnO also contributes to the irreversible loss of the composites since it reacts with Li-ions to form Li_2O, effectively trapping lithium within its structure and within the SEI layer. FTIR data for 80-W-10-N are similar to 85-W-10-N and hence is not shown. The fact that this reaction occurs in the first cycle accounts for the lack of SnO peaks in the first cycle FTIR plot (Fig. 5). As a result of the above reaction occurring during the first cycle discharge, it is probable that very fine Sn particles form. Although samples for FTIR analysis were prepared in a glove box, some air contact is inevitable during transfer to the FTIR chamber for collection of FTIR spectra. This can lead to the formation of SnO as is evidenced in the FTIR spectra of the sample in the 25th cycle.

3.4. SEM analysis

SEM microscopy conducted on these composites show a much more homogeneous sample surface for those composites obtained by wet milling (Fig. 6b and c) than those that were dry milled (Fig. 6a and d). This is thought to be due to a more even distribution of the energy that occurs during wet HEMM as well as a lowering of the overall temperature due to the presence of the solvent. As a result, it is possible that the elements are much more homogeneously mixed resulting in a homogeneous composite. SEM micrographs were also collected for the wet milled 85-W-10-N composite sample after the 1st (Fig. 7a) and 25th cycles (Fig. 7b). It is evident here that the composite has already experienced some structural failure seen by the presence of cracks. The sample observed after the 25th cycle, shows

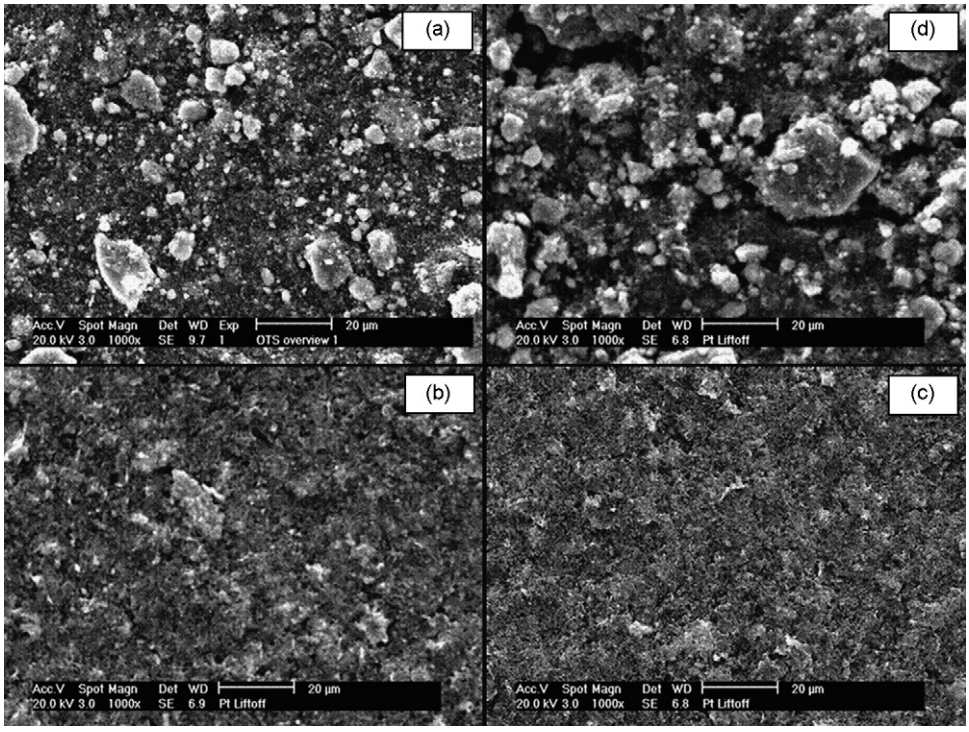

Fig. 6. SEM micrographs of all four, as prepared, composite electrodes: (a) 75-D-10, (b) 80-W-10-N, (c) 85-W-10-N and (d) 90-D-10.

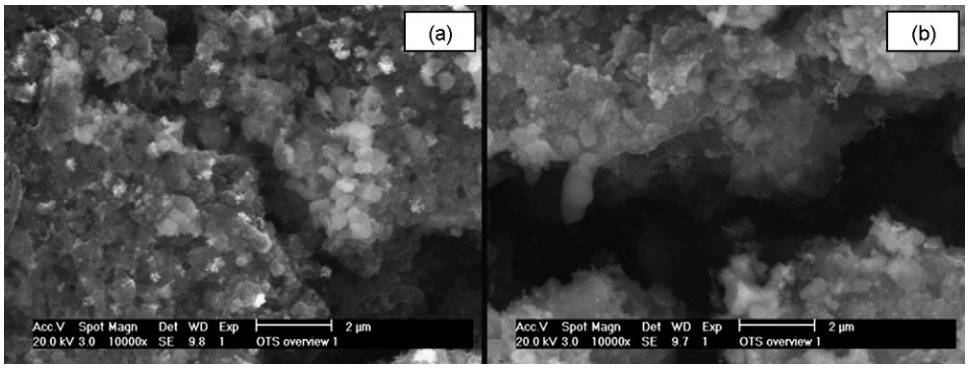

Fig. 7. SEM micrographs (10,000×) of 85-W-10-N after: (a) 1st cycle and (b) 25th cycle.

cracks that seem to have penetrated much deeper into the sample than those seen for the sample collected after one cycle (see Fig. 7a and b). This indicates that prolonged cycling continues to degrade the structural integrity of the electrode. This claim is reinforced by the continual loss of capacity seen in Fig. 2 for this sample.

3.5. Addition of toluene as a milling solvent

Toluene was investigated as a possible solution to the several problems observed, particularly the formation of SnO when using NMP as a solvent during the wet milling process. For these experiments, all preparations mirrored those used for preparing wet milled sample using NMP. The only difference being that toluene was evaporated off by placing the milled slurry into a drying oven set at 85 °C for 6 h, and the dried sample was used to prepare electrodes similar to that described above using precursors derived from the dry HEMM method. The sample composition 85C–15[$Si_{0.66}Sn_{0.34}$], which exhibited the best overall performance, was therefore synthesized using toluene to compare the electrochemical performance to those samples milled in NMP and under dry conditions.

Fig. 8 is an X-ray plot of the 85C–15[$Si_{0.66}Sn_{0.34}$] composition collected on samples at varying milling times, milled employing various conditions and solvents (see Table 2). Upon closer inspection it is evident that there is a significant difference in the intensity of the graphite peak between the sample milled for 10 h in NMP and 10 h in toluene. The graphite peak is much smaller for the latter case, and as all other conditions were the same, the cause of this amorphization must be a result of the solvent used. In fact, the viscosity of NMP is much greater than that of toluene (1.65 mPa s at 25 °C [56] versus 0.56 mPa s at 25 °C [57], respectively), which would account for the appearance of a more amorphous graphite peak in the case of the less viscous toluene solvent.

Fig. 9 compares the electrochemical performance of the 85C–15[$Si_{0.66}Sn_{0.34}$] composition at varying milling times, conditions, and solvents. The composition 85-W-5-T yields the best overall performance as it exhibits the highest overall capacity after 30 cycles of ~470 mAh g^{-1} coupled with an irreversible loss of ~50.5%, and loss per cycle of the same order as the same sample milled using NMP as the solvent (see Table 2). In examination of the differential capacity plot of this composite

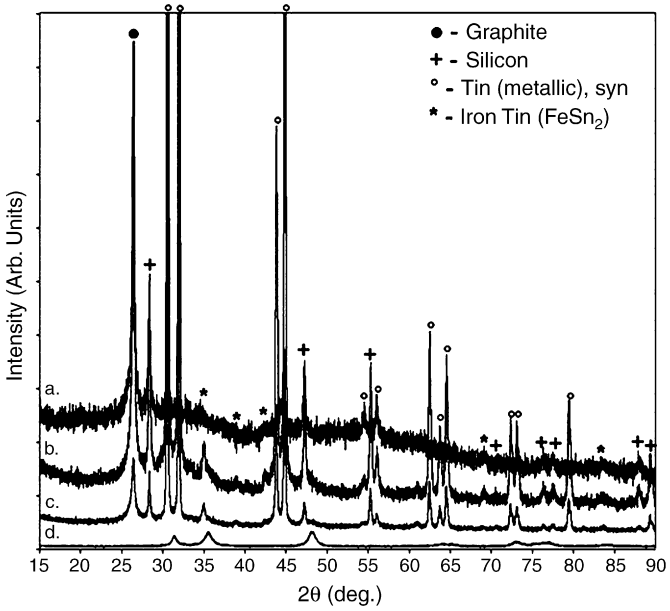

Fig. 8. XRD patterns of 85C–15[$Si_{0.66}Sn_{0.34}$] (mol%) composition at varying milling times, conditions and solvents: (a) 85-W-10-N, (b) 85-W-5-T, (c) 85-W-10-T and (d) 85-D-10.

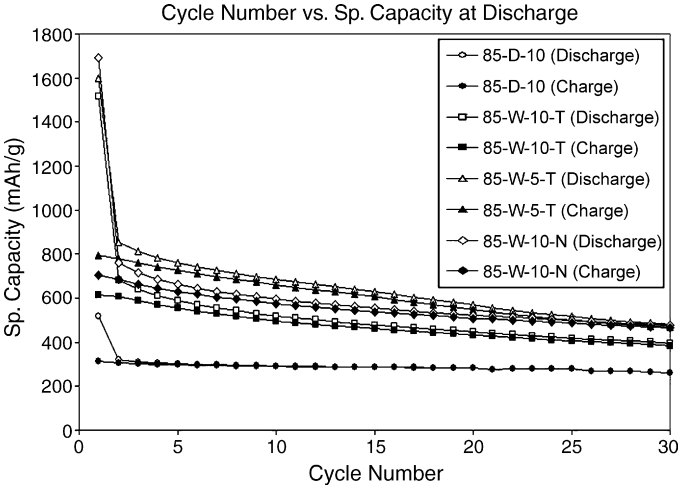

Fig. 9. Specific capacity vs. cycle numbers of 85C–15[$Si_{0.66}Sn_{0.34}$] (mol%) composition at varying milling times, conditions and solvents cycled at a rate of 250 μA cm^{-2}.

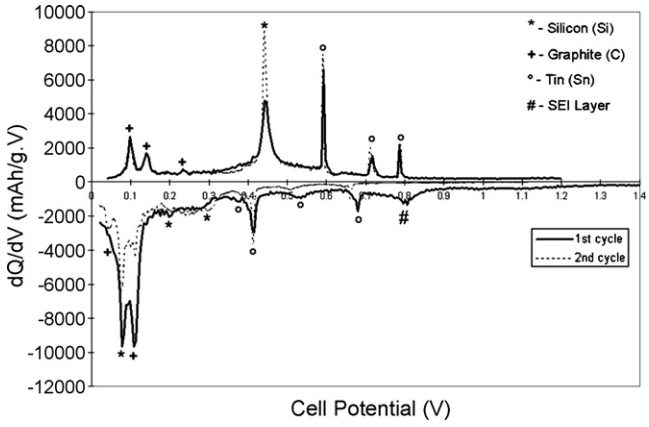

Fig. 10. Differential capacity vs. cell potential curves of 85-W-5-T composite electrode after first and second cycles.

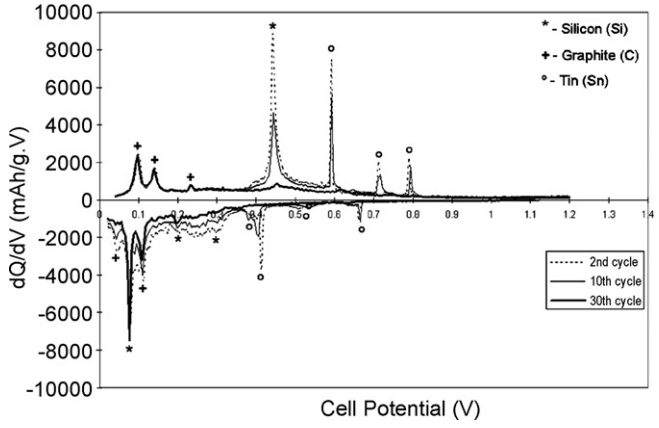

Fig. 11. Differential capacity vs. cell potential curves of 85-W-5-T composite electrode after 2nd, 10th and 30th cycles.

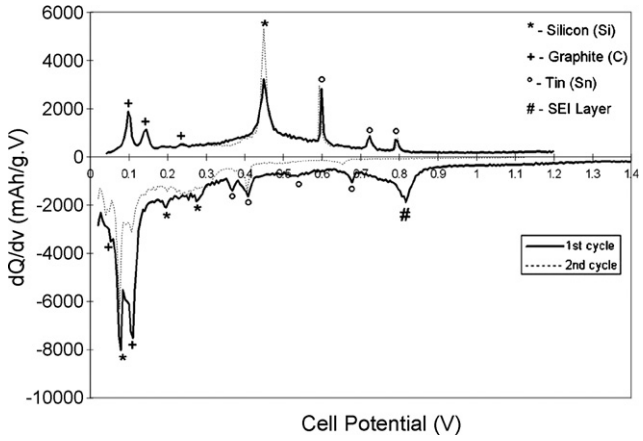

Fig. 13. Differential capacity vs. cell potential curves of 85-W-10-T composite electrode after first and second cycles.

(Figs. 10 and 11), one can see that there are peaks corresponding to the reaction of Li-ions with Si at ∼0.45, 0.3, 0.2 and 0.08 V [46]. There are also peaks present for graphite at ∼0.22, 0.15, 0.10 and 0.07 V, and for Sn at 0.79, 0.73, 0.66, 0.53, 0.42 and 0.38 V [49].

Fig. 12 is an FTIR plot comparing the 25 cycles of the two samples 85-W-10-N and 85-W-5-T. The most important aspect of this plot is the fact that the sample milled in toluene shows an absence of any amorphous SnO phases. This, coupled with the $dQ\,dV^{-1}$ plots, further reinforces the assertion that SnO is not present in the samples milled in toluene. However, in the case of the samples milled in toluene, SnO is not the single contributing factor controlling the irreversible loss. One sees no improvement in the irreversible loss for the 85-W-10-T sample as compared to the 85-W-10-N sample (Table 2). Thus, another factor must be contributing to this loss as it has been determined that SnO is not present in the samples milled in toluene. The $dQ\,dV^{-1}$ plot of the 85-W-10-T sample (Fig. 13) shows a much

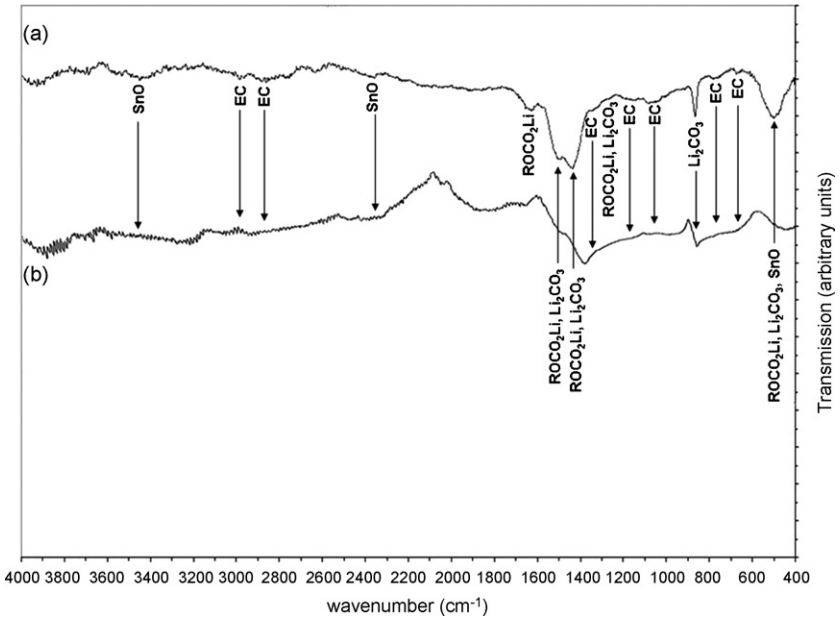

Fig. 12. FTIR transmission mode plots of: (a) 85-W-10-N (25 cycles) and (b) 85-W-5-T (25 cycles).

larger peak for the formation of an SEI layer than that of the 85-W-10-N (Fig. 3). Though no SnO is present in the 85-W-10-T sample, the fact it possesses a larger SEI peak accounts for the similarities in irreversible loss between these two materials. In a similar manner, the fact that the 85-W-5-T sample has a lower irreversible loss than the 85-W-10-T sample is evident from the reduced SEI peak, seen when comparing the $dQ\,dV^{-1}$ plots of these two samples (Figs. 10 and 13, respectively). Therefore, it is important to remember that, while the irreversible loss can be reduced through the elimination of a contaminant such as SnO, the role of the SEI layer must not be overlooked as it has a significant effect upon performance.

Both the irreversible loss and loss per cycle problems may be addressed through the implementation of Li-ion containing polymer coatings as well as lithium carbonated containing coatings as these materials can reduce the thickness of the SEI layer while still providing stability to the battery. The use of an elastomeric binder may also provide the flexibility for volume expansion of Si and Sn that occur upon lithiation. The overall reversible specific capacity of the composite should also be increased. This can be done by using a composite that is comprised of a greater amount of material that possesses a higher theoretical capacity. Thus, in order to accomplish this, the amount of Sn in this system can be reduced to increase Si. As Si has a much greater theoretical capacity (4197 mAh g^{-1}, gravimetric) than Sn (994 mAh g^{-1}, gravimetric) it is logical to increase the amount of Si as it holds the possibility for resulting in a much greater capacity yield. At the same time, one must restrict the addition of Sn to the minimum amount to prevent SiC formation.

4. Conclusions

Based upon the performed experiments there are several conclusions that can be made:

(1) The composition 85-W-5-T yields the best overall performance as it exhibits the highest overall capacity after 30 cycles of ∼470 mAh g^{-1} coupled with an irreversible loss of ∼50.5%, and loss per cycle of the same order as the same sample milled using NMP as the solvent.
(2) SnO most likely formed during wet milling where NMP was used as a solvent due to the reaction of Sn with NMP during HEMM to cleave some of the doubly bonded oxygens, rendering them available for reaction with Sn to form the oxide.
(3) Amorphous carbon does form as a direct result of prolonged milling time that the powders undergo during the HEMM process.
(4) SiC does not form in either material due to the fact that Sn and Si are immiscible and Sn prevents the formation of SiC by acting as a diffusion barrier to the reaction between Si and graphite.

Acknowledgement

The authors would like to thank NASA (NAG3-2640) for financial support of this research.

References

[1] T. Nagaura, K. Tozawa, Prog. Batteries Solar Cells 9 (1990) 209.
[2] T. Tran, J. Feikert, X. Song, K. Kinosbita, J. Electrochem. Soc. 142 (1995) 3297.
[3] J.P. Maranchi, Fundamental experimental studies of amorphous silicon thin film anodes for lithium-ion applications, Ph.D. Thesis, 2004.
[4] J.O. Besenhard, M. Hess, P. Komenda, Solid State Ionics 40/41 (1990) 525.
[5] M. Winter, J.O. Besenhard, Electrochim. Acta 45 (1999) 31.
[6] J.O. Besenhard, J. Yang, M. Winter, J. Power Sources 68 (1997) 87.
[7] R.A. Huggins, Solid State Ionics 113–115 (1998) 57.
[8] J. Yang, M. Winter, J.O. Besenhard, Solid State Ionics 90 (1996) 281.
[9] J.O. Besenhard, P. Komenda, A. Paxinos, E. Wudy, Solid State Ionics 18/19 (1986) 823.
[10] B.A. Boukamp, G.C. Lesh, R.A. Huggins, J. Electrochem. Soc. 128 (1981) 725.
[11] L.Y. Beaulieu, K.W. Eberman, R.L. Turner, L.J. Krause, J.R. Dahn, Electrochem. Solid-State Lett. 4 (2001) A137.
[12] O. Mao, R.L. Turner, I.A. Courtney, B.D. Fredericksen, M.I. Buckett, L.J. Krause, J.R. Dahn, Electrochem. Solid State Lett. 2 (1999) 3.
[13] A.M. Wilson, J.N. Reimers, E.W. Fuller, J.R. Dahn, Solid State Ionics 74 (1994) 249.
[14] W. Xing, A.M. Wilson, G. Zank, J.R. Dahn, Solid State Ionics 93 (1997) 239.
[15] A.M. Wilson, W. Xing, G. Zank, B. Yates, J.R. Dahn, Solid State Ionics 100 (1997) 259.
[16] I. Kim, G. Blomgren, P. Kumta, Electrochem. Solid-State Lett. 7 (2004) A44.
[17] I. Kim, P. Kumta, G. Blomgren, Electrochem. Solid-State Lett. 3 (2000) 493.
[18] I. Kim, G. Blomgren, P. Kumta, Electrochem. Solid-State Lett. 6 (2003) A157.
[19] O. Crosnier, T. Brousse, X. Devaux, P. Fragnaud, D.M. Schleich, J. Power Sources 84 (2001) 169.
[20] W. Xing, A.M. Wilson, K. Eguchi, G. Zank, J.R. Dahn, J. Electrochem. Soc. 144 (1997) 2410.
[21] A.M. Wilson, B.M. Way, J.R. Dahn, T. van Buuren, J. Appl. Phys. 77 (1995) 2363.
[22] A.M. Wilson, J.R. Dahn, J. Electrochem. Soc. 142 (1995) 326.
[23] A.M. Wilson, G. Zank, K. Eguchi, W. Xing, J.R. Dahn, J. Power Sources 68 (1997) 195.
[24] S. Bourderau, T. Brousse, D.M. Schleich, J. Power Sources 81/82 (1999) 233.
[25] H. Li, X. Huang, L. Chen, Z. Wu, Y. Liang, Electrochem. Solid-State Lett. 2 (1999) 547.
[26] C.S. Wang, G.T. Wu, X.B. Zhang, Z.F. Qi, W.Z. Li, J. Electrochem. Soc. 145 (1998) 2751.
[27] H. Li, Q. Wang, L. Shi, L. Chen, X. Huang, Chem. Mater. 14 (2002) 103.
[28] M. Winter, J.O. Besenhard, J.H. Albering, J. Yang, M. Wachtler, Prog. Batteries Battery Mater. 17 (1998) 208.
[29] P. Poizot, S. Laruelle, S. Grugeon, L. Dupont, J.M. Tarascon, Nature 407 (2000) 496.
[30] A. Netz, R.A. Huggins, W. Weppner, J. Power Sources 119–121 (2003) 95–100.
[31] R.A. Huggins, Solid State Ionics 152–153 (2002) 61–68.
[32] L.M.L. Fransson, J.T. Vaughey, K. Edstrom, M.M. Thackeray, J. Electrochem. Soc. 150 (2003) A86–A91.
[33] E. Frackowiak, S. Gautier, H. Gaucher, S. Bonnamy, F. Béguin, Carbon 37 (1999) 61.
[34] T. Ishihara, A. Kawahara, H. Nishigushi, M. Yoshio, Y. Takita, J. Power Sources 97/98 (2001) 129.
[35] A.S. Claye, J.E. Fischer, C.B. Huffmann, A.G. Rinzler, R.E. Smalley, J. Electrochem. Soc. 147 (2000) 2845.
[36] O. Mao, R.A. Dunlap, J.R. Dahn, J. Electrochem. Soc. 146 (1999) 405.
[37] O. Mao, J.R. Dahn, J. Electrochem. Soc. 146 (1999) 414.
[38] O. Mao, J.R. Dahn, J. Electrochem. Soc. 146 (1999) 423.

[39] K.D. Kepler, J.T. Vaughey, M.M. Thackeray, Electrochem. Solid-State Lett. 2 (1999) 307.
[40] M.M. Thackeray, J.T. Vaughey, A.J. Kahaian, K.D. Keplar, R. Benedek, Electrochem. Commun. 1 (1999) 111.
[41] K.D. Keplar, J.T. Vaughey, M.M. Thackeray, J. Power Sources 81/82 (1999) 383.
[42] J.T. Vaughey, J. O'Hara, M.M. Thackeray, Electrochem. Solid-State Lett. 3 (2000) 13.
[43] G.M. Ehrlich, C. Durand, X. Chen, T.A. Hugener, F. Speiss, S.L. Suib, J. Electrochem. Soc. 147 (2000) 886.
[44] L.Y. Beaulieu, K.C. Hewitt, R.L. Turner, A. Bonakdarpour, A.A. Abdo, L. Christensen, K.W. Eberman, L.J. Krause, J.R. Dahn, J. Electrochem. Soc. 150 (2003) A149–A156.
[45] P.N. Kumta, D. Gallet, A. Waghray, G.E. Blomgren, M.P. Setter, J. Power Sources 72 (1998) 91–98.
[46] I. Kim, P.N. Kumta, J. Power Sources 136 (2004) 145–149.
[47] I. Kim, G.E. Blomgren, P.N. Kumta, J. Power Sources 130 (2004) 275–280.
[48] Z.G. Yang, L.L. Shaw, Nanostruct. Mater. 7 (1996) 873–886.
[49] A. Ulus, Yu. Rosenburg, L. Burnstein, E. Peled, J. Electrochem. Soc. 149 (2002) A635–A643.
[50] D. Aurbach, A. Nimberger, B. Markovsky, E. Levi, E. Sominski, A. Gedanken, Chem. Mater. 14 (2002) 4155–4163.
[51] M. Winter, J. Besenhard (Eds.), Handbook of Battery Materials, Weinheim, Wiley-VCH, New York, 1999, pp. 419–456.
[52] J.S. Gnanaraj, M.D. Levi, E. Levi, G. Salitra, D. Aurbach, J.E. Fischer, A. Claye, J. Electrochem. Soc. 148 (2001) A525–A536.
[53] D. Aurbach, J.S. Gnanaraj, M.D. Levi, E.A. Levi, J.E. Fisher, A. Claye, J. Power Sources 97/98 (2001) 92–96.
[54] S. Geniès, R. Yazami, J. Garden, J.C. Frison, Synth. Mater. 93 (1998) 77–82.
[55] Y. Idota, T. Kubota, A. Matsufuji, Y. Maekawa, T. Miyasaka, Science 276 (1997) 1395.
[56] https://fscimage.fishersci.com/msds/08690.htm.
[57] David R. Lide (Ed.), Viscosity of Liquids, CRC Handbook of Chemistry and Physics, 87th ed., Taylor and Francis, Boca Raton, FL, 2007, Internet Version.